Article

Seeing mesoatomic distortions in soft-matter crystals of a double-gyroid block copolymer

Xueyan Feng[1], Christopher J. Burke[2], Mujin Zhuo[1], Hua Guo[1], Kaiqi Yang[1], Abhiram Reddy[2], Ishan Prasad[3], Rong-Ming Ho[4], Apostolos Avgeropoulos[5], Gregory M. Grason[2]* & Edwin L. Thomas[1]*

Supramolecular soft crystals are periodic structures that are formed by the hierarchical assembly of complex constituents, and occur in a broad variety of 'soft-matter' systems[1]. Such soft crystals exhibit many of the basic features (such as three-dimensional lattices and space groups) and properties (such as band structure and wave propagation) of their 'hard-matter' atomic solid counterparts, owing to the generic symmetry-based principles that underlie both[2,3]. 'Mesoatomic' building blocks of soft-matter crystals consist of groups of molecules, whose sub-unit-cell configurations couple strongly to supra-unit-scale symmetry. As yet, high-fidelity experimental techniques for characterizing the detailed local structure of soft matter and, in particular, for quantifying the effects of multiscale reconfigurability are quite limited. Here, by applying slice-and-view microscopy to reconstruct the micrometre-scale domain morphology of a solution-cast block copolymer double gyroid over large specimen volumes, we unambiguously characterize its supra-unit and sub-unit cell morphology. Our multiscale analysis reveals a qualitative and underappreciated distinction between this double-gyroid soft crystal and hard crystals in terms of their structural relaxations in response to forces—namely a non-affine mode of sub-unit-cell symmetry breaking that is coherently maintained over large multicell dimensions. Subject to inevitable stresses during crystal growth, the relatively soft strut lengths and diameters of the double-gyroid network can easily accommodate deformation, while the angular geometry is stiff, maintaining local correlations even under strong symmetry-breaking distortions. These features contrast sharply with the rigid lengths and bendable angles of hard crystals.
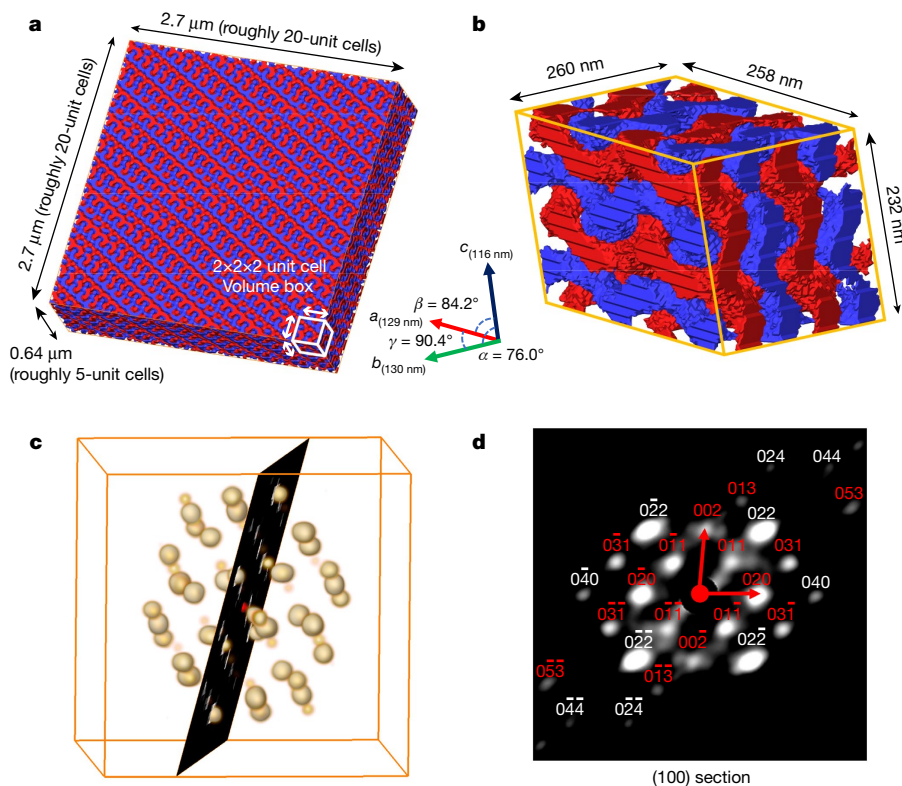
Three-dimensional (3D) tomographic imaging is the definitive experimental technique for determining the morphology of complex nanostructures. Tomography can be performed with a variety of microscopic methods, provided that there is a suitable match between the imaging resolution and the feature size. For block copolymer (BCP) structures in which periodicities are typically in the 10–100-nm regime, with domain features on the scale of 2–20 nm, electron microscopy techniques are generally required. To date, nearly all 3D tomograms of bulk-phase BCPs have been made using transmission electron microscopy (TEM) tomography[4–6]. Although powerful, this technique is quite limited with regard to the range of sample thicknesses, and inevitably incurs both sample deformation from microtomy and information loss associated with the restriction of tilt angles[7].

Here we use the considerable advantages afforded by a wholly distinct approach to the tomography of nanostructured 3D morphologies: slice-and-view scanning electron microscopy (SVSEM; also named focused ion beam scanning electron microscopy, or FIB-SEM)[8–10]. Crucially, by comparison with TEM tomography, SVSEM tomography can provide a much larger reconstruction in all three spatial dimensions, facilitating 3D analysis of volumes many orders of magnitude larger than those of the typical unit cell and allowing 3D fast Fourier transform (FFT) from selected volumes within the overall reconstruction. We study a polystyrene-polydimethylsiloxane (PS-PDMS) double-gyroid BCP. The double gyroid is composed of two independent, interpenetrating enantiomorphic tubular networks of one type of block (PDMS), separated by a slab-like domain[11,12] (whose shape is loosely approximated by the G minimal surface[13]) that is constituted by the second, majority block (PS). Although a double gyroid would nominally be classified as cubic (cDG; space group of $Ia\bar{3}d$) in accordance with equilibrium theories of BCPs[14,15], a more critical analysis of the morphology

[1]Department of Material Science and Nano Engineering, Rice University, Houston, TX, USA. [2]Department of Polymer Science and Engineering, University of Massachusetts, Amherst, MA, USA. [3]Department of Chemical Engineering, University of Massachusetts, Amherst, MA, USA. [4]Department of Chemical Engineering, National Tsing Hua University, Hsinchu, Taiwan. [5]Department of Materials Science Engineering, University of Ioannina, University Campus Dourouti, Ioannina, Greece. *e-mail: grason@mail.pse.umass.edu; elt@rice.edu

Fig. 1 | Supra-unit cell structure of the PS-PDMS double-gyroid tubular network phase. a, Real-space SVSEM reconstruction of PDMS domains (rendered red and blue), corresponding to about 2,000 unit cells of the (non-cubic) double gyroid. The white box at the bottom right highlights the size of a 2 × 2 × 2 unit-cell subvolume. **b**, A magnified view showing a different triclinic 2 × 2 × 2 volume cropped from within the large volume shown in panel **a**. The binarized (PS versus PDMS) raw SVSEM voxels are further divided into red and blue PDMS voxel networks, with the PS domains rendered transparent. The triclinic unit cell parameters (a, b, c, α, β and γ) measured from real space are also shown. **c**, Rendering of the 3D FFT analysis of a region containing approximately 160 unit cells, with Bragg-like spots highlighted as quasi-spheriodal volumes, showing how the data intersect with a (100) plane. The central 000 peak is indicated as a red spot. See Supplementary Video 2 for an animated view of the 3D diffractogram. **d**, 2D logarithmic intensity plot of a (100) section from the 3D Fourier data. In addition to the allowed $\{220\}_{tDG}$, $\{400\}_{tDG}$, $\{420\}_{tDG}$ and $\{440\}_{tDG}$ reflections (indexed in white), there are $\{110\}_{tDG}$, $\{200\}_{tDG}$, $\{310\}_{tDG}$ and $\{530\}_{tDG}$ reflections that would be forbidden in the cubic double gyroid (indexed in red).

reveals that the slow solution-cast material organizes into distinct triclinic variants of the cubic phase.

A 3D rendering of a $2.70 \times 2.70 \times 0.64\ \mu m^3$ volume containing about 2,000 unit cells from within a large double-gyroid monodomain is shown in Fig. 1a. The two constituent tubular PDMS networks (shown in red and blue)—which each enclose about 20% of the total volume—are defect-free, consistent with their disjointed segmentation. Prior standard small-angle X-ray scattering (SAXS) and TEM analysis indicated that this sample has a cDG structure[16]; however, careful analysis of the morphology throughout the 'ultra-large' volumes accessible to 3D SVSEM reconstruction reveals a decidedly non-cubic unit-cell symmetry. Figure 1b shows an experimental reconstructed 2 × 2 × 2 unit-cell volume, including triclinic unit-cell parameters. The symmetry of the particular cells in this grain deviates greatly from cubic, with the largest and smallest lattice parameters differing by 12% (for example, 130 nm versus 116 nm) and with pairs of translation vectors deviating by up to 14° from orthogonality. The synchronized slices normal to the [001] direction from the experimental reconstruction and from the corresponding deformed self-consistent field (SCF) double-gyroid model are compared in Supplementary Video 1. As shown in Extended Data Fig. 1, unit-cell parameters exhibit only small deviations throughout a given many-cubic micrometre-scale grain. Other grains exhibit distinct triclinic variants. These triclinic variants deviate from cubic symmetry by up to about 20% in both length and angle. We denote this morphology as 'variable triclinic double gyroid' (vtDG) in order to indicate unit cells that are essentially coherent within grains, but vary substantially from grain to grain. As shown in Extended Data Fig. 2, directions and magnitudes of deviations from cubic symmetry in distinct regions of the sample are uncorrelated with slicing directions, ruling out the possibility that the measured anisotropy is an artefact of SVSEM imaging or reconstruction.

Structural symmetries can also be assessed using 3D FFT of the SVSEM data. The detailed distribution of intensity from a particular (hkl) Bragg plane depends on the orientation and spacing distributions of the (hkl) planes within the volume of the sample transformed. We use selected
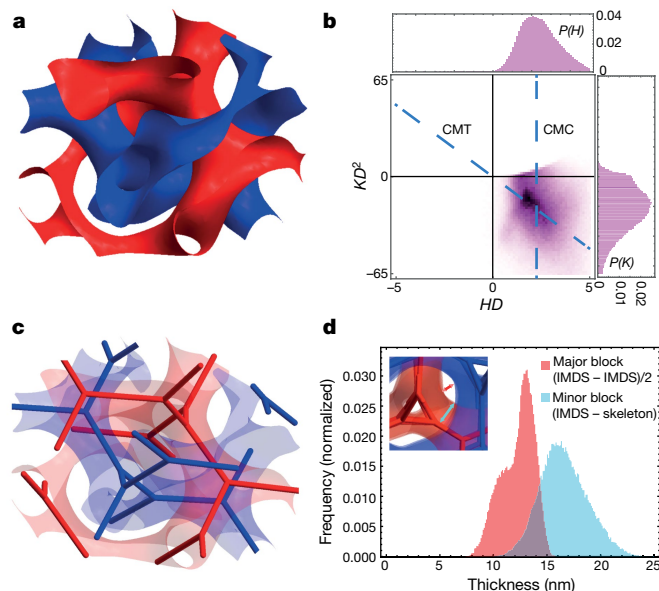

Fig. 2 | Sub-unit cell IMDS curvature and distance metrics. a, Bragg-filtered reconstruction of the IMDS for one unit cell (for a description of the IMDS isosurface, see Methods). **b**, Graph plotting the normalized Gaussian (K) and mean (H) curvatures of the IMDS and their respective probability functions (P), based on a region of 35 unit cells. The curvatures are normalized by $<D> = 130$ nm (the average lattice parameter cell dimension measured by SAXS). The diagonal and vertical dashed blue lines indicate the curvature distributions for a constant minimal G surface thickness (CMT) IMDS and a constant mean curvature (CMC) IMDS. **c**, The same unit cell as in panel **a** but with the IMDS made semi-transparent, revealing the two skeletal graphs that are found by a thinning algorithm (see Methods). **d**, Distance distributions for the minority and majority domains. The minority-block thickness is measured from the IMDS to the closest distance to the skeletal graph. The majority-block thickness is measured as half the distance from a point on the red IMDS to the closest point on the blue IMDS.
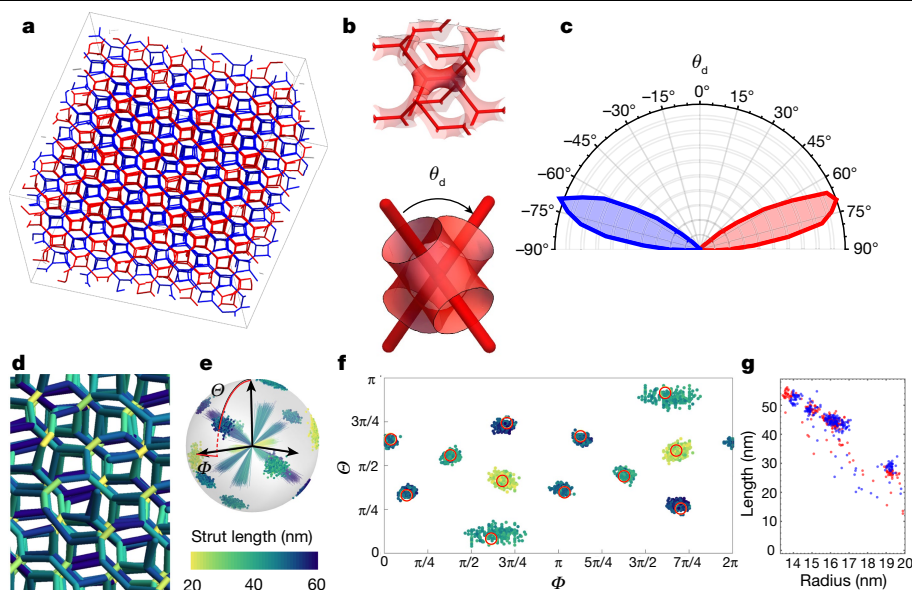
Fig. 3 | Sub-unit cell length and angular metrics. a, Region of roughly 100 unit cells, where a topological thinning of the segmented SVSEM tomogram has been used to create the two skeletal graphs of the double-gyroid structure. The viewing direction is approximately [100]. **b**, A small region from the theoretical cubic unit cell, depicting the skeletal graph and the surrounding IMDS, highlighting an internode strut with one cubic unit cell (top) and its dihedral rotation when viewed along the strut (bottom). The solid dark red central IMDS piece contains two nodes of the graph, and by viewing along the strut connecting the nodes, one can measure the dihedral angle, θ_d. **c**, Polar plot of the dihedral angle for the red ($\langle\theta_d\rangle = +70.9°$) and blue ($\langle\theta_d\rangle = -70.8°$) experimental networks, showing the narrow distribution of angles in each network. **d**, A portion of the skeletal graph from panel **a**, with the struts coloured according to their length, showing a factor of roughly three in variability. **e**, Spherical plot of the strut lengths versus their orientation in the laboratory frame. **f**, The same data projected onto a Mercator plot, where Θ and Φ are the polar and azimuthal angles, respectively, of the strut orientation as shown in **e**. The <110> strut directions of a cDG lattice are shown as red circles. **g**, Inverse correlation between strut length and mean 'tube' radius of the IMDS measured at the midpoint along the strut (with red and blue colours indicating two distinct networks), showing the transverse contraction (dilation) upon length stretching (compression) of tubular struts.

volume diffraction (SVD)—the SEM analogue of the selected area diffraction (SAD) used in TEM analysis—in order to choose the location, shape and size of the volume to be transformed from within the larger reconstructed sample volume (see Methods). The most intense allowed cubic $Ia\bar{3}d$ reflections—the {211} and {220} families—are used to define a transformation matrix that fits a triclinic lattice in order to maximize the overall intensity values at the deformed reciprocal lattice points (Fig. 1c). Measurement of the distorted reciprocal cell parameters from SVD are in perfect correspondence with the real-space measurements. Notably, inspection of the 3D SVD pattern shows intensity spots located at 'symmetry-forbidden' Bragg positions if indexed with the cubic $Ia\bar{3}d$ space group. Forbidden reflections (see, for example, Fig. 1d) become allowed when distortions break the centring translation, screw and glide symmetries of the cubic structure. Although the experimental intensities of the most prominent of these 'forbidden' reflections are two to three orders of magnitude below those of the {211} reflections, they are $10–10^5$ greater in magnitude than the 'symmetry-allowed' {321} and {400} reflections. The occurrence of these relatively strong 'forbidden' reflections indicates that the vtDG morphology does not simply correspond to an affine deformation of the cDG morphology, but rather to the non-affine rearrangement of the morphology at the sub-unit-cell scale. We note that distortions (attributed to solvent shrinkage forces) have resulted in the appearance of forbidden reflections in prior SAXS studies of double-gyroid structures in both bulk and thin-film BCPs[17–20].

We also analyse the sub-unit-cell morphology of the PS-PDMS double gyroid, first focusing on the shape of the intermaterial dividing surface (IMDS) and on domain thicknesses. Although the resolution of the raw SVSEM tomogram is limited by the roughly 3-nm width of image voxels (as seen in Fig. 1b), the intragrain coherence of 3D morphology over large multicell volumes enables quantitative analysis of the 'average' unit cell at higher resolution. This is accomplished by Fourier averaging of the raw greyscale SVSEM data through application of a 3D Bragg

filter (see Methods)—an approach that is well established in 2D high-resolution TEM[21]. An isosurface constructed from the Bragg-filtered SVSEM data shows the two IMDS regions, each containing PDMS and enclosing roughly 20% of the unit volume (Fig. 2a), allowing measurement of the mean (H) and Gaussian (K) curvature distributions (Fig. 2b).

Heuristically, we can compare this experimental H versus K distribution with two limiting theoretical geometries: a constant matrix thickness (CMT) surface, which is surface displaced (normally) by a constant from the G minimal surface[13]; or a constant mean curvature (CMC) surface[22]. Although a CMC shape has been suggested[13,22] on the grounds that it minimizes the IMDS area for a fixed volume fraction[11,23], the CMT surface minimizes the entropic penalty of variable stretching of the majority component at the expense of a slight increase in the interfacial area[24]. The curvature distributions for mathematical cDG surfaces of both types are shown in Extended Data Fig. 3a, b. The curvature distribution of a CMC surface is localized to a vertical band $HD = 2.23$, while that of a CMT surface follows Steiner's linear relationship, $HD = -(t/2D)KD^2$ or $HD = -0.103KD^2$ (where D is the cell repeat length and t is the constant thickness of the slab-like matrix domain)[1]. Relative to these reference surfaces, the experimental curvature distribution is closer to the CMC distribution. Also shown in Extended Data Fig. 3c–f are the H and K distributions for SCF theoretical calculations of cDG as a function of segregation strength. Although the IMDS shape of these model equilibrium states is always intermediate to the CMC and CMT shapes in terms of the curvature distribution, we note that the shapes are relatively CMC-like in weakly segregated gyroids and trend towards CMT-like when interblock repulsions are increased. This observation, in combination with the CMC-like distribution measured in Fig. 2b, might suggest that the experimental IMDS shape is inherited from a state in which the PS domain vitrifies and fixes the shape of the ordering structure during solvent evaporation. It remains far from clear, however, if and how closely the shape of the partially solvated and non-equilibrium
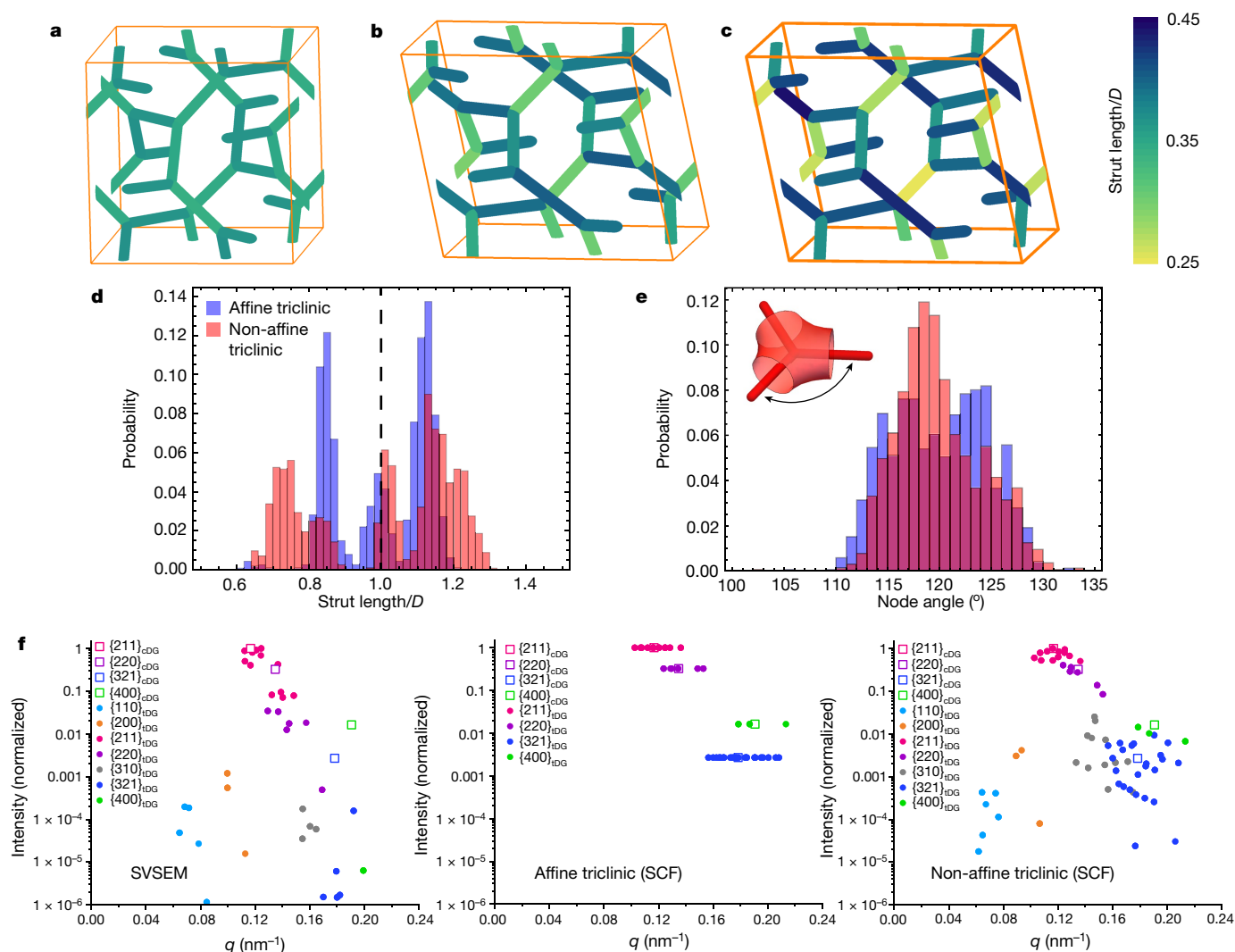
Fig. 4 | Models of sub-unit cell morphology. a–c, Orthographic views of portions of skeletal graphs for cubic (**a**), affine triclinic (**b**) and non-affine triclinic (**c**) models derived from equilibrium SCF calculations with cubic or triclinic symmetry. Here the colour indicates the strut length between nodes, normalized by the mean cell repeat length D. **d**, Probability distributions for the strut length/mean cell repeat length computed for affine and non-affine triclinic models. **e**, Probability distributions for internode angles for the same computed networks, with colours as in panel **d**. **f**, Intensity of reflections (circles) made by 3D FFT of: the SVSEM reconstruction (left; roughly 160 unit cells); the affine triclinic SCF model (centre; 64 unit cells); and the non-affine triclinic SCF model (right; 64 unit cells). For reference, the allowed peaks for cDG are plotted with open squares.

double-gyroid morphology can be modelled by an equilibrium theory for neat diblocks. We note that the IMDS shape of a BCP double gyroid has been analysed previously[4–6], yet resolution limitations for the IMDS curvature of the TEM tomography measurement made identification of the surface shape signature inaccessible.

The inhomogeneous geometry of the double gyroid implies a heterogeneous distribution of domain thicknesses[12,25], corresponding to variable degrees of chain extension throughout the structure. To characterize the variable thickness of the minority domains, we derive a skeletal graph from the SVSEM reconstruction; this graph consists of 1D struts threading through geometric 'centres' of tubular domains and meeting at threefold junctions (Fig. 2c)[26]. We define a 'minor block thickness' as the shortest distance from a point on the IMDS to the interior skeleton, while a 'major block thickness' is half of the shortest distance from a point on one IMDS to the IMDS of the opposing network (Fig. 2d, inset). Distributions of the minor (PDMS) and major (PS) block thicknesses are shown in Fig. 2d. Previous explanations for double-gyroid formation in BCP have emphasized that the constraints involved in packing polymer blocks at constant density require variation in the stretch length, most

prominently derived from the greater distance from the IMDS to the threefold junction node than from the corresponding IMDS-to-sketelon distance at the mid-portion of an internode strut[24,27]. This notion of 'packing frustration' is consistent with the broad spread of minor-block length. However, the measured distribution of thicknesses for the major PS block also exhibits substantial spread, indicating that—contrary to the present heuristic picture[24]—packing of the majority block is also frustrated. Non-uniform matrix thickness thus arises as a consequence of the 'tug of war' between majority-block stretching and the countervailing forces that favour more uniform minor-block lengths, as well as from the drive towards area-minimizing IMDS shapes[23,28], consistent with the more CMC-like distribution observed in Fig. 2b.

Although the IMDS shape and domain thickness are necessarily inhomogeneous even in the ideal cDG, the internode struts in the ideal cDG are uniform in length and all orient along <110> directions. The experimental network morphology can be further analysed using the skeletal graphs (Fig. 3a). We first consider the dihedral angle (Fig. 3b). In an ideal cDG network this angle is ±70.5° (modulo 180°), where the sign characterizes the chirality of the two enantiomorphic single-gyroid

networks[26]. Remarkably, the experimental dihedrals for the positive and negative networks deviate little (with a root-mean-squared variance of less than 11°) from the ideal cubic geometry values (Fig. 3c). We also show (Extended Data Fig. 4) for the interstrut angles in the experimental vtDG a deviation of only about 20% from the perfect threefold coordination (120°) of cDG. This degree of local angular order in the PDMS networks contrasts starkly with the pronounced variability in the length of tubular struts as measured by skeletal edges. Strut length can vary by up to 300% (Fig. 3d). Figure 3e, f analyses the lengths of PDMS struts according to their orientation, and indicates a strong correlation between the orientation and the 12 <110> directions of a cDG graph. Struts in a given orientation are relatively homogeneous in length, but show prominent length variations between distinct orientations—exceptionally large given the more modest (roughly 20%) discrepancy between triclinic and cubic cell geometry. Notably, in Fig. 3g we show concomitant contraction/dilation of the transverse tubular radius with stretching/compression of the strut length.

To understand the origin of the anomalously large variability among PDMS strut lengths versus the relative constancy of strut angles, we consider the microdomain structures and their associated skeletal graphs derived from SCF models of the tDG. The first model, affine triclinic, is generated by affinely deforming the SCF cDG structure (Fig. 4a) into a particular tDG shape equal to that of the experimentally determined unit cell (Fig. 4b). A second model, non-affine triclinic, instead uses the same experimental triclinic cell boundary conditions to compute an equilibrium SCF double-gyroid morphology (Fig. 4c). As shown in Fig. 4d, e, the affine triclinic deformation of the double gyroid leads to spread of the strut lengths and angles by roughly 10–20%, comparable in scale to the imposed strains deforming the cubic cell to triclinic symmetry. Remarkably, if instead we consider the predicted double-gyroid morphology that equilibrates within the same triclinic cell, the network structure adopts an increased degree of length dispersity (Fig. 4d)—well beyond the nominal lengths derived from cubic to triclinic distortion—and yet a reduced degree of angle dispersity (Fig. 4e). Moreover, comparison of the spectrum of Fourier peaks from the experimental versus the SCF affine triclinic and non-affine triclinic models reveals extraordinary correspondence between the experimental structure and the non-affine triclinic model (Fig. 4f).

Taken together, these observations suggest a strong thermodynamic coupling of sub-unit-cell morphology to symmetry breaking at the supra-unit-cell scale of the double-gyroid phase. Strut lengths (and diameters) are relatively soft and thus easily accommodate deformation, presumably through relatively rapid intradomain transport of polymer chains. By contrast, the angular geometry of the gyroid network is stiff, favouring local correlations that are maintained even under strong symmetry-breaking deformations. This suggests a heuristic model for the non-affine structure of symmetry-broken soft-matter networks, consisting of periodic networks of tensed struts (so-called Steiner networks, which are 1D analogues of Plateau borders)[29,30] that adjust lengths locally yet maintain force-balancing angular coordination at the nodes, in order to minimize the stretching that occurs in response to imposed changes in unit-cell symmetry.

Our observations have been made possible by the accessibility of ultralarge volumes to SVSEM tomography, in combination with the Bragg averaging of selected volumes, in order to achieve enhanced resolution of sub-unit-cell features. New distance and angle metrics applied to the complex double-gyroid phase allow deeper insight into the complex energetic competition, as reflected in the distinctive structural distortions in actual samples that invariably result from solvent evaporation and grain boundary incompatibility. The symmetry-breaking distortions are predicted to have impacts on, for example, the photonic/phononic band properties of double-gyroid assemblies[2,31]. Our research opens up a new way of unambiguously characterizing a variety of soft-matter systems that assemble under different processing conditions into a variety of soft crystals (beyond networks), illuminating their formation mechanisms, supra-cell and sub-cell structures and structure–property relationships.

Online content

Any methods, additional references, Nature Research reporting summaries, source data, extended data, supplementary information, acknowledgements, peer review information; details of author contributions and competing interests; and statements of data and code availability are available at https://doi.org/10.1038/s41586-019-1706-1.

1. Hyde, S. et al. *The Language of Shape* 141–197 (Elsevier Science, 1997).
2. Urbas, A. M., Maldovan, M., DeRege, P. & Thomas, E. L. Bicontinuous cubic block copolymer photonic crystals. *Adv. Mater.* **14**, 1850–1853 (2002).
3. Lee, J. H. et al. 25th anniversary article: ordered polymer structures for the engineering of photons and phonons. *Adv. Mater.* **26**, 532–569 (2014).
4. Laurer, J. H. et al. Microstructural analysis of a cubic bicontinuous morphology in a neat SIS triblock copolymer. *Macromolecules* **30**, 3938–3941 (1997).
5. Jinnai, H. et al. Direct measurement of interfacial curvature distributions in a bicontinuous block copolymer morphology. *Phys. Rev. Lett.* **84**, 518–521 (2000).
6. Li, Z. H. et al. Linking experiment and theory for three-dimensional networked binary metal nanoparticle-triblock terpolymer superstructures. *Nat. Commun.* **5**, 3247 (2014).
7. Ercius, P., Alaidi, O., Rames, M. J. & Ren, G. Electron tomography: a three-dimensional analytic tool for hard and soft materials research. *Adv. Mater.* **27**, 5638–5663 (2015).
8. Feng, X. Y., Guo, H. & Thomas, E. L. Topological defects in tubular network block copolymers. *Polymer* **168**, 44–52 (2019).
9. Hayworth, K. J. et al. Ultrastructurally smooth thick partitioning and volume stitching for large-scale connectomics. *Nat. Methods* **12**, 319–322 (2015).
10. Narayan, K. & Subramaniam, S. Focused ion beams in biology. *Nat. Methods* **12**, 1021–1031 (2015).
11. Schick, M. Avatars of the gyroid. *Physica A* **251**, 1–11 (1998).
12. Schroeder-Turk, G. E., Fogden, A. & Hyde, S. T. Bicontinuous geometries and molecular self-assembly: comparison of local curvature and global packing variations in genus-three cubic, tetragonal and rhombohedral surfaces. *Eur. Phys. J. B* **54**, 509–524 (2006).
13. Hajduk, D. A. et al. The gyroid—a new equilibrium morphology in weakly segregated diblock copolymers. *Macromolecules* **27**, 4063–4075 (1994).
14. Matsen, M. W. The standard Gaussian model for block copolymer melts. *J. Phys. Condens. Matter* **14**, R21–R47 (2002).
15. Cochran, E. W., Garcia-Cervera, C. J. & Fredrickson, G. H. Stability of the gyroid phase in diblock copolymers at strong segregation. *Macromolecules* **39**, 2449–2451 (2006).
16. Lo, T. Y. et al. Phase transitions of polystyrene-b-poly(dimethylsiloxane) in solvents of varying selectivity. *Macromolecules* **46**, 7513–7524 (2013).
17. Toombes, G. E. S. et al. A re-evaluation of the morphology of a bicontinuous block copolymer-ceramic material. *Macromolecules* **40**, 8974–8982 (2007).
18. Faber, M., Hofman, A. H., Loos, K. & ten Brinke, G. Highly ordered structure formation in RAFT-synthesized PtBOS-b-P4VP diblock copolymers. *Macromol. Rapid Commun.* **37**, 911–919 (2016).
19. Chavis, M. A., Smilgies, D. M., Wiesner, U. B. & Ober, C. K. Widely tunable morphologies in block copolymer thin films through solvent vapor annealing using mixtures of selective solvents. *Adv. Funct. Mater.* **25**, 3057–3065 (2015).
20. Dolan, J. A. et al. Controlling self-assembly in gyroid terpolymer films by solvent vapor annealing. *Small* **14**, 1802401 (2018).
21. Henderson, R., Baldwin, J. M., Downing, K. H., Lepault, J. & Zemlin, F. Structure of purple membrane from halobacterium halobium: recording, measurement and evaluation of electron micrographs at 3.5 Å resolution. *Ultramicroscopy* **19**, 147–178 (1986).
22. Große-Brauckmann, K. Gyroids of constant mean curvature. *Exp. Math.* **6**, 33–50 (1997).
23. Thomas, E. L., Anderson, D. M., Henkee, C. S. & Hoffman, D. Periodic area-minimizing surfaces in block copolymers. *Nature* **334**, 598–601 (1988).
24. Matsen, M. W. & Bates, F. S. Origins of complex self-assembly in block copolymers. *Macromolecules* **29**, 7641–7644 (1996).
25. Schroeder, G. E., Ramsden, S. J., Christy, A. G. & Hyde, S. T. Medial surfaces of hyperbolic structures. *Eur. Phys. J. B* **35**, 551–564 (2003).
26. Prasad, I., Jinnai, H., Ho, R. M., Thomas, E. L. & Grason, G. M. Anatomy of triply-periodic network assemblies: characterizing skeletal and inter-domain surface geometry of block copolymer gyroids. *Soft Matter* **14**, 3612–3623 (2018).
27. Olmsted, P. D. & Milner, S. T. Strong segregation theory of bicontinuous phases in block copolymers. *Macromolecules* **31**, 4011–4022 (1998).
28. Grason, G. M. The packing of soft materials: molecular asymmetry, geometric frustration and optimal lattices in block copolymer melts. *Phys. Rep.* **433**, 1–64 (2006).
29. Ivanov, A. O. & Tuzhilin, A. A. *Minimal Networks: The Steiner Problem and Its Generalizations* (CRC Press, 1994).
30. Alex, J. & Grosse-Braukmann, K. *Periodic Steiner networks minimizing length*. Preprint at http://arxiv.org/abs/1705.02471 (2017).
31. Fruchart, M. et al. Soft self-assembly of Weyl materials for light and sound. *Proc. Natl Acad. Sci. USA* **115**, E3655–E3664 (2018).

Article

Methods

Material and sample preparation

We synthesized the polystyrene-poly(dimethylsiloxane) (PS-PDMS) diblock copolymer[16] by sequential anionic polymerization of styrene and hexamethylcyclotrisiloxane. The polymer has number average molecular weights of 43.5 kg mol^{-1} (for PS) and 29.0 kg mol^{-1} (for PDMS), with an overall composition of 40% PDMS (by volume) and a polydispersity index of 1.04. The sample studied was cast slowly (over the course of one week) from a 10 wt% solution (2 ml) in toluene. After drying, the sample was heated to 60 °C for 3 days in a vacuum in order to remove any residual solvent.

On the basis of characteristic 2D TEM and radially averaged SAXS, the PS-PDMS diblock copolymer has been reported to have a double-gyroid morphology[16]. We further characterized the small piece of sample that we used for SVSEM with the synchrotron X-ray at Sector 12-ID-B of the Advanced Photo Source in the Argonne National Laboratory. Given the SAXS pattern (Extended Data Fig. 5), the structure can indeed be nominally associated with a double-gyroid morphology, with an average cubic repeat of $D = 130$ nm. However, we observe a prominent low q peak associated with the {110} planes that is forbidden for the cubic $Ia\bar{3}d$ space group. Given the size of the incident X-ray beam and the sample thickness, this SAXS pattern must come from about 10^9 unit cells. Before SVSEM imaging, the sample was attached to a 45° SEM stub with double-sided conductive carbon tape, and the outer surface was then coated with a 50-nm layer of platinum.

Slice-and-view SEM data acquisition

Extended Data Fig. 6 shows the workflow involved in SVSEM. This is a tomographic method enabled by advances in ion milling, monochromated field emission electron beams and electron imaging detectors, as well as by precise stage motion and sophisticated software routines for correlation and registration of the image stack[32–34]. During data collection (Extended Data Fig. 6a), ion milling is combined with electron imaging (Extended Data Fig. 7a): an incident high-energy ion beam is used to make an impact on and mill away a thin slice of the near-surface region of the sample (Extended Data SFig. 7b, i); then an electron beam is directed at the surface and a secondary-electron image is recorded (Extended Data Fig. 7b, ii). This ion-slice, electron-image sequence is repeated until a sufficient thickness of the sample has been serially imaged. The 3D tomogram is then reconstructed by vertical stacking of the aligned 2D SEM images. Three large-volume tomographic data sets from distinct double-gyroid grains are available at an online data repository (https://doi.org/10.7275/wv24-3j62).

We used a Thermo Fisher Helios NanoLab 660 SEM/FIB DualBeam system for data acquisition. A focused gallium-ion (Ga$^+$) beam with an energy of 30 KeV and a relatively low beam current of 80 pA was used to mill the sample surface in order to minimize damage from the FIB beam[35]. A 1-KeV electron beam with beam current of 50 pA was used to image the sample surface with a through lens (TLD) secondary-electron detector (secondary-electron images taken with different incident energies are shown in Extended Data Fig. 8). Notably, the stronger scattering from the higher atomic number of silicon atoms in the PDMS and the resulting additional secondary-electron emission is sufficient to provide excellent intrinsic contrast between the PS and PDMS domains without staining. We used X-shaped fiducials to register the FIB and secondary-electron images during the automatic slice-and-view process, and drilled a deep hole (or holes) into the sample along the direction normal to the observing surface with FIB (at an acceleration voltage of 30 kV and beam current of 0.23 nA) for fine registration of secondary-electron images (for details, see Extended Data Fig. 9a–c). For FIB slicing, we set the slice thickness at 3 nm. Further monitoring during FIB image acquisition found the actual slice thicknesses to be 2.96 ± 0.01 nm per slice (for details, see Extended Data Fig. 9d). A potential relative rotation of SEM images during SVSEM

acquisition was also monitored and excluded (Extended Data Fig. 10 and Supplementary Video 3).

SCFT and IMDS models

We performed self-consistent (mean) field theory calculations of diblock copolymer melts using a polymer self-consistent field (PSCF) code (http://pscf.cems.umn.edu/) as in ref. [36] for cubic double gyroid (cDG) and non-affine triclinic double gyroid (natDG) morphologies, with a single-chemical-parameters family: that is, a volume fraction f, product of interblock repulsion χ, and degree of polymerization N. The initial density-field profiles for a double gyroid were based on the example files distributed with the software, and later targeted for the 40% minority (PDMS) and 60% majority (PS) volume fractions.

For the natDG we generated an initial density field that is identical to the experimentally reported lattice dimensions. We performed SCFT calculations by iteratively changing the density fields while calculating the free energy at each step and progressing towards a free-energy minimum. Then, for cDG and natDG, we further adjusted the lattice dimensions while maintaining the unit-cell length ratios in order to find a metastable density field subject to imposed symmetry constraints. For natDG, we fixed $a/b = 0.97/1$, $a/c = 1.10/1$ and angles α, β, γ as 75.9°, 84.7°, 89.1°, which derive from the unit-cell parameters computed from the optimal (inverse) reciprocal lattice dimension from experimental SVSEM measurements, and are therefore close to those of the local volume region shown in Fig. 1b. Here we did not attempt to achieve an equivalent segregation strength (χN) to match PS-PDMS systems, because it is unclear which equilibrium values correspond best to the conditions in which the sample (as it is undergoing solvent evaporation) becomes ordered but remains fluid in both domains. Instead, we aimed to capture the basic mechanism of the sub-unit cell non-affine structure without imposing a close match in interblock repulsion. Hence, for fixed symmetries (cDG or natDG) we consider the cell dimension that minimizes the free energy for fixed ratios of unit-cell dimensions and angles. The affinely sheared triclinic DG (atDG) was generated from cDG, by applying a transformation matrix that consisted of lattice vectors matching the natDG at the same composition and interaction parameters. Finally, for each of the cDG, atDG and natDG, we generated image stacks of the density fields for further geometric analysis.

For the IMDS models in Extended Data Fig. 3a, b, we generated the CMC surface of a tubular double-gyroid network by using Surface Evolver[37] and following the procedure in ref. [22]. Thus we generated discrete CMC surfaces corresponding to the IMDS by minimizing the area and energy associated with a target mean curvature (H_0) for the IMDS (that is, $\int(H(x) - H_0)^2 dA$, where $H(x)$ is the mean curvature of the surface at point x, and dA is the infinitesimal area at point x) by imposing volume constraints such that the minority component volume enclosed by the tubular networks is 40% of the cubic cell. Similarly, for the CMT IMDS, we took a discretized surface of the gyroid minimal surface and then pushed off all points by the same distance along the normal ($\pm\hat{n}$), such that the resulting volume enclosed by surfaces on either side of the minimal surface matched the 60% volume fraction of PS in the unit cell. See the supporting software at the online data repository (https://doi.org/10.7275/wv24-3j62) for details on generating image stacks from density fields.

Morphological analysis

The following subsections describe the steps (Extended Data Fig. 6b–g) that ultimately led to a detailed geometric analysis (Extended Data Fig. 6h). The custom computer codes used for these tasks are noted in each subsection, and the file 'README.txt' distributed with the supporting software outlines further instructions regarding the use of these codes with source data. All of the supporting software codes and 'README.txt' are at the online data repository (https://doi.org/10.7275/wv24-3j62).

Visualization of 3D volumes using raw secondary-electron images. See Extended Data Fig. 6b, c. Visualization was carried out with Avizo software from Thermo Fisher. The raw secondary-electron images of the PS-PDMS BCP have excellent intrinsic contrast. We further segmented the 3D tomogram by setting the initial voxel intensity threshold in order to manually define a portion of the bright, higher-intensity region (PDMS) as well as a portion of a darker, lower-intensity region (PS). We then calculated the position of the boundary between the brighter and darker regions using a gradient algorithm. The watershed operation[38] was then applied to fill in the two types of region. This procedure avoided the creation of any internal islands within each type of domain. After using a given threshold, we checked the volume fraction of each block against the known value from nuclear magnetic resonance (NMR: 40/60 PDMS/PS). Using these segmented images, we can reconstruct a 3D volume as coloured PDMS networks with a transparent PS matrix.

Selected-volume diffraction of SVSEM reconstruction. See Extended Data Fig. 6d–f. Because SVSEM captures the structure over large dimensions in every direction of the sample, it enables high-resolution analysis in reciprocal space, affording local observation of the orientation and magnitude of distinct Bragg-like intensity regions without loss of phase information. Before transforming the real-space volume data into Fourier space, we applied a Hanning window[39] in order to reduce artefacts in the FFT associated with discontinuities at the sample boundary. The filtered intensity of each real-space image voxel is given by:

$$I(u,v,w) = \frac{1}{8}\left[1-\cos\left(\frac{2\pi(u-1)}{N_u}\right)\right]\left[1-\cos\left(\frac{2\pi(v-1)}{N_v}\right)\right]$$
$$\times\left[1-\cos\left(\frac{2\pi(w-1)}{N_w}\right)\right]I_0(u,v,w)$$

where $I_0(u,v,w)$ is the original unfiltered voxel intensity; N_u, N_v and N_w are the number of voxels in each dimension; and (u,v,w) denote the integer voxel positions in the real-space data. After applying the Hanning window, the voxel intensity data were Fourier transformed in order to obtain the reciprocal space representation, $F(i,j,k)$.

To perform further selected-volume-diffraction (SVD) analysis, we needed an indexed reciprocal space lattice that fits with the FFT data. To achieve this, we started with a small portion of a cDG reciprocal space lattice, $\mathbf{G}_{hkl}$. We included the two families of non-forbidden reciprocal lattice vectors with the smallest magnitude of $\mathbf{G}_{hkl}$, {211} and {220}. These cubic reciprocal-space vectors have a magnitude of $|\mathbf{b}_i| = 2\pi/130 \text{ nm}^{-1}$, where 130 nm is the average unit-cell length estimated from SAXS. In order to fit the generated lattice to the FFT data, we constructed a smooth interpolation of the FFT data, making it into a cubic spline interpolation, $F_{smooth}(k_x, k_y, k_z)$. The coordinates of each FFT pixel are given by $(k_x, k_y, k_z) = (i\delta k_x, j\delta k_y, k\delta k_z)$, where $\delta k_x = 2\pi/\delta x$, $\delta k_y = 2\pi/\delta y$ and $\delta k_z = 2\pi/\delta z$, and δx, δy and δz are the real-space voxel dimensions. We then fit the reciprocal lattice to the FFT interpolation. In doing so, we assumed that the structure was periodic and that the real-space lattice was affinely transformed from a cubic lattice. Applying a linear transformation $x_i \to x'_i = \Lambda_{ij}x_j$, where the nine matrix elements Λ_{ij} are independent, we could transform from a cubic to a triclinic unit cell. For the transformation to be linear, we required that $k'_i x'_i = k_i x_i$, so $k'_i = k_j \Lambda_{ji}^{-1}$. The goal of our fitting procedure was to find the elements of Λ^{-1} that transform the cubic reciprocal lattice vectors to lie on the peaks of the FFT. Specifically, we optimized the matrix elements Λ_{ij} in order to maximize the summed value of interpolated intensity at the deformed reciprocal lattice vectors, $\sum_{\mathbf{k}\in\mathbf{G}_{hkl}} F_{smooth}(\Lambda_{ji}^{-1}k_j)$, where $\mathbf{G}_{hkl}$ are the reciprocal lattice vectors of the cubic double gyroid lattice. Having found the indexed (deformed) reciprocal lattice that fits the FFT data, we applied a targeted Bragg filter to the volume data. The Bragg filter was applied in Fourier space with a mask of Gaussian windows, while each

window was centred on the selected reciprocal-space lattice point. The Bragg mask is given by:

$$B(i,j,k) = \sum_{\mathbf{k}\in\mathbf{G}'_{hkl}} \exp\left[\frac{(i\delta k_x - k_x)^2}{2\sigma_x^2} + \frac{(j\delta k_y - k_y)^2}{2\sigma_y^2} + \frac{(k\delta k_z - k_z)^2}{2\sigma_z^2}\right]$$

Where σ_x, σ_y and σ_z are widths of Gaussian windows in the mask and $\mathbf{G}'_{hkl}$ are the set of vectors in the (non-cubic) reciprocal lattice that locate each of the intensity peaks in the 3D FFT. We applied the filter pointwise to the FFT data and then applied an inverse FFT in order to obtain the filtered real-space volume data for further analysis. To carry out SVD analysis, we selected reciprocal-space lattice points on the basis of the corresponding overall intensity of each diffraction family of the FFT data and their associated cubic q value (Extended Data Fig. 11). Here we chose reciprocal-space lattice points such that their corresponding diffraction families have an overall intensity greater than 10^{-7} (normalized by the strongest $\{211\}_{tDG}$ family) and their associated cubic q values are smaller than 0.2 nm^{-1} to make the Bragg filtering mask (that is, the $\{110\}_{tDG}$, $\{200\}_{tDG}$, $\{210\}_{tDG}$, $\{211\}_{tDG}$, $\{220\}_{tDG}$, $\{310\}_{tDG}$, $\{321\}_{tDG}$, $\{400\}_{tDG}$ families), while the standard deviation of the Gaussian window is two pixels (that is, $\sigma_x = 2\delta k_x$, $\sigma_y = 2\delta k_y$, $\sigma_z = 2\delta k_z$). A comparison of the 3D FFT pattern of the raw volume data and the 3D FFT pattern of the volume data after SVD treatment is shown in Extended Data Fig. 6d, e. See the supporting software 2.

Network skeletal graphs and analysis. See Extended Data Fig. 6g, h (with regard to dihedral angles, strut lengths and strut orientations). Using ImageJ (https://imagej.nih.gov/ij/), we binarized the greyscale image-stack data in order to identify the tubular networks formed by the minority domains, and separated them from the majority-block-filled matrix by using a threshold such that the volume fractions of the two binary components matched with the experimentally reported volume fractions. Note that although the same analysis could be applied to post-Bragg filtered data, the data in Fig. 3 consider a larger volume than is accessible to memory limitations of FFT filtering in Mathematica (see https://doi.org/10.7275/wv24-3j62). Hence, in order to analyse large-volume networks, we extracted the skeleton directly from the raw SVSEM data (comparative analyses of skeletons from pre- and post-filtered data in a smaller volume confirm that Bragg filtering has a negligible impact on network statistics).

We then reduced these networks into 1D skeletal graphs—that is, straight-line bonds that connect nodes which are threefold coordinated or higher; no fourfold or higher-fold nodes were identified in this way (indicating the absence of topological defects[8]). The initial task of reducing filtered 3D volume data into 1D lines was done using the inbuilt skeletonization feature in ImageJ. This procedure followed ref.[40], and it reduces binarized volume data into a 1D curve (also referred as a medial axis) that is a collection of voxels. To identify the skeletal graphs, we subjected the 1D curve to further refinements. We did this using a custom Mathematica code, whereby we first converted the voxel collections into a graph by taking the voxel coordinates as vertices, and then connected each voxel to its adjacent neighbours in a $3\times3\times3$ voxel neighbourhood. For the next refinement, we fixed the vertices that lie on the boundary and iteratively removed vertices that have only one nearest neighbour which effectively removed branches of the 1D curve that did not connect to a node. Finally, we converted the remaining 1D curve into a straight line of bonds by iteratively removing vertices with two neighbours and then connecting them to one another. The end of this process usually results in having small clusters of vertices at the site of a node, which we rectified by replacing them with a single vertex, ultimately resulting in the skeletal graph with the same topology of the network that we started out with.

We then applied an optimization procedure to ensure that the skeleton lines lie along the regions of maximal density in the 3D volume data. This was achieved using an algorithm described in ref.[26], which

Article

defines an optimization functional in $\Phi = \sum_{\langle ij \rangle} \frac{1}{L_{ij}} \int_i^j ds\, \phi(\mathbf{x})$ that averages the local intensity $\phi(\mathbf{x})$ over the skeleton bonds, where $\langle ij \rangle$ denotes the skeleton bond connecting $\mathbf{x}_i$ and $\mathbf{x}_j$, and s represents the arc length along each skeletal bond. We used a cubic spline interpolation to create the density (or intensity f) function $\phi(\mathbf{x})$, based on reconstructed 3D volume data from images. We maximized this function with respect to node positions $\mathbf{x}_i$ in order to optimize the skeleton position over density ϕ. We analysed the structure of the optimized skeletal graphs by calculating the skeleton dihedral angles and the length and orientation of the bonds that make up the graphs. For a given triplet of consecutive bonds, we defined the two planes and their normal as $\hat{\mathbf{n}}_{\alpha\beta} = (\hat{\mathbf{r}}_\alpha \times \hat{\mathbf{r}}_\beta)/|(\hat{\mathbf{r}}_\alpha \times \hat{\mathbf{r}}_\beta)|$ and $\hat{\mathbf{n}}_{\beta\gamma} = (\hat{\mathbf{r}}_\beta \times \hat{\mathbf{r}}_\gamma)/|(\hat{\mathbf{r}}_\beta \times \hat{\mathbf{r}}_\gamma)|$, where $\hat{\mathbf{r}}_\alpha$, $\hat{\mathbf{r}}_\beta$ and $\hat{\mathbf{r}}_\gamma$ are the unit vectors along the bonds. The dihedral angle is defined as the angle between these plane normals, with $\sin\theta = (\hat{\mathbf{n}}_{\alpha\beta} \times \hat{\mathbf{n}}_{\beta\gamma}) \cdot \hat{\mathbf{r}}_\beta$, $\cos\theta = \hat{\mathbf{n}}_{\alpha\beta} \cdot \hat{\mathbf{n}}_{\beta\gamma}$. We calculated this measure for all consecutive triplets of bonds in the skeletal graph. We also calculated the bond length as $l_{ij} = |\mathbf{r}_{ij}|$ where $\mathbf{r}_{ij} = \mathbf{x}_i - \mathbf{x}_j$, with i and j denoting the nodes (end points) of the struts, and the spherical angle coordinates Θ and Φ describing the length and orientation anisotropy. The node angle $\psi = \cos^{-1}(\hat{\mathbf{r}}_\alpha \cdot \hat{\mathbf{r}}_\beta)$ is computed for each of the three pairs (α, β) of struts that meet at a single node; this is done for all nodes in the unit cell. Data from this analysis are presented as a polar histogram of dihedral angles in Fig. 3c, a histogram of node angles in Extended Data Fig. 4, Mercator plots of orientation in Fig. 3e, f, and anisotropy of strut length in Fig. 4d. See the supporting software 3, 4.

Calculation of curvature. See Extended Data Fig. 6g, h (with regard to IMDS curvature). We computed the mean curvature (H) and Gaussian curvature (K) of the IMDS. The IMDS is represented as a triangulated mesh, which we identified by finding a surface of the linear interpolation of density data at ϕ_{40} that separated the 3D volume into three types of domain with 20%, 20% and 60% volume.

We further used two-step conditioning by first applying an edge-length regularization to the mesh, and then constraining the mesh vertices to lie on the isosurface of a third-order interpolation of the density to ensure that mesh vertices represent a surface that is at least second-order differentiable. To regularize the triangle edge lengths, we minimized a regularization functional defined as $F_{\text{reg}} = \sum_{\langle ij \rangle} (L_{ij} - \bar{L})^2$. We optimized this functional via a gradient-descent approach by taking the gradient with respect to the triangle vertex positions, and applied a constraint such that all resulting vertices lie on the surface by subtracting the component of gradient parallel to vertex normal. To constrain the mesh vertices, we created a third-order Hermite interpolation of density ϕ and we constrained each triangle vertex to lie along the $\phi = 0.4$ isosurfaces within this interpolation. We accomplished this by minimizing $(\phi - 0.4)^2$ for each vertex, again using the gradient-descent approach. We finally used the patch curvature function in the Matlab File Exchange developed by D.-J. Kroon (https://www.mathworks.com/matlabcentral/fileexchange/32573-patch-curvature) in order to compute curvatures on the optimized triangulated mesh that represents the IMDS. This algorithm calculated the principal curvatures κ_1 and κ_2 associated with each triangulated vertex by fitting a paraboloid to that vertex and its nearest neighbours, with the paraboloid axis constrained along the vertex normal. From the principal curvatures, the mean curvature $H = \frac{(\kappa_1 + \kappa_2)}{2}$ and Gaussian curvature $K = \kappa_1 \kappa_2$ can be calculated for each vertex. Curvature-distribution data are shown in Fig. 2b and Extended Data Fig. 3. See also the supporting software 5, 6, 7.

Calculation of skeleton–IMDS and IMDS–IMDS distances and strut diameters. See Extended Data Fig. 6g, h (with regard to the skeleton–IMDS and IMDS–IMDS distances). We used the optimized IMDS triangulated mesh and discretized skeletal graph to compute skeleton–IMDS and IMDS–IMDS distances and the effective diameters of the tubular networks. We carried out skeletal-graph discretization by choosing a discretization length $d = \langle l_b \rangle/100$, where $\langle l_b \rangle$ is the average bond length and for each bond we chose l_b/d evenly spaced points along the bond. We calculated distances between the skeleton and IMDS by finding the nearest skeleton point for each vertex on the IMDS triangulated mesh, and IMDS–IMDS distances by considering separately the two IMDS surfaces resulting from individual networks and finding the nearest vertex in one IMDS from each vertex on the other. To calculate the effective strut diameter, we found the (quasi-ellipsoidal) 1D intersection of the computed IMDS and a 2D plane that bisects a strut. An 'average tube radius' is computed by dividing the length of the 1D path (that is, the circumference) by 2π. The skeleton–IMDS and IMDS–IMDS distances are plotted in Fig. 2d, and the effective strut diameter versus strut length in Fig. 3g. See also the supporting software 8, 9.

Data availability

SVSEM and SCF modelling data are available at https://doi.org/10.7275/wv24-3j62.

Code availability

Supporting software codes are available at https://doi.org/10.7275/wv24-3j62.

32. Cantoni, M. & Holzer, L. Advances in 3D focused ion beam tomography. *MRS Bull.* **39**, 354–360 (2014).
33. Kotula, P. G., Rohrer, G. S. & Marsh, M. P. Focused ion beam and scanning electron microscopy for 3D materials characterization. *MRS Bull.* **39**, 361–365 (2014).
34. Wilson, J. R. et al. Three-dimensional reconstruction of a solid-oxide fuel-cell anode. *Nat. Mater.* **5**, 541–544 (2006).
35. Kim, S., Park, M. J., Balsara, N. P., Liu, G. & Minor, A. M. Minimization of focused ion beam damage in nanostructured polymer thin films. *Ultramicroscopy* **111**, 191–199 (2011).
36. Arora, A. et al. Broadly accessible self-consistent field theory for block polymer materials discovery. *Macromolecules* **49**, 4675–4690 (2016).
37. Brakke, K. A. The surface evolver. *Exp. Math.* **1**, 141–165 (1992).
38. Beucher, S. & Meyer, F. in *Mathematical Morphology in Image Processing* (ed. Dougherty, E. R.) 433–481 (CRC Press, 1993).
39. Oppenheim, A. V. & Schafer, R. W. *Discrete-Time Signal Processing* (Prentice-Hall, 1999).
40. Lee, T. C., Kashyap, R. L. & Chu, C. N. Building skeleton models via 3-D medial surface axis thinning algorithms. *CVGIP Graph. Models Image Proc.* **56**, 462–478 (1994).
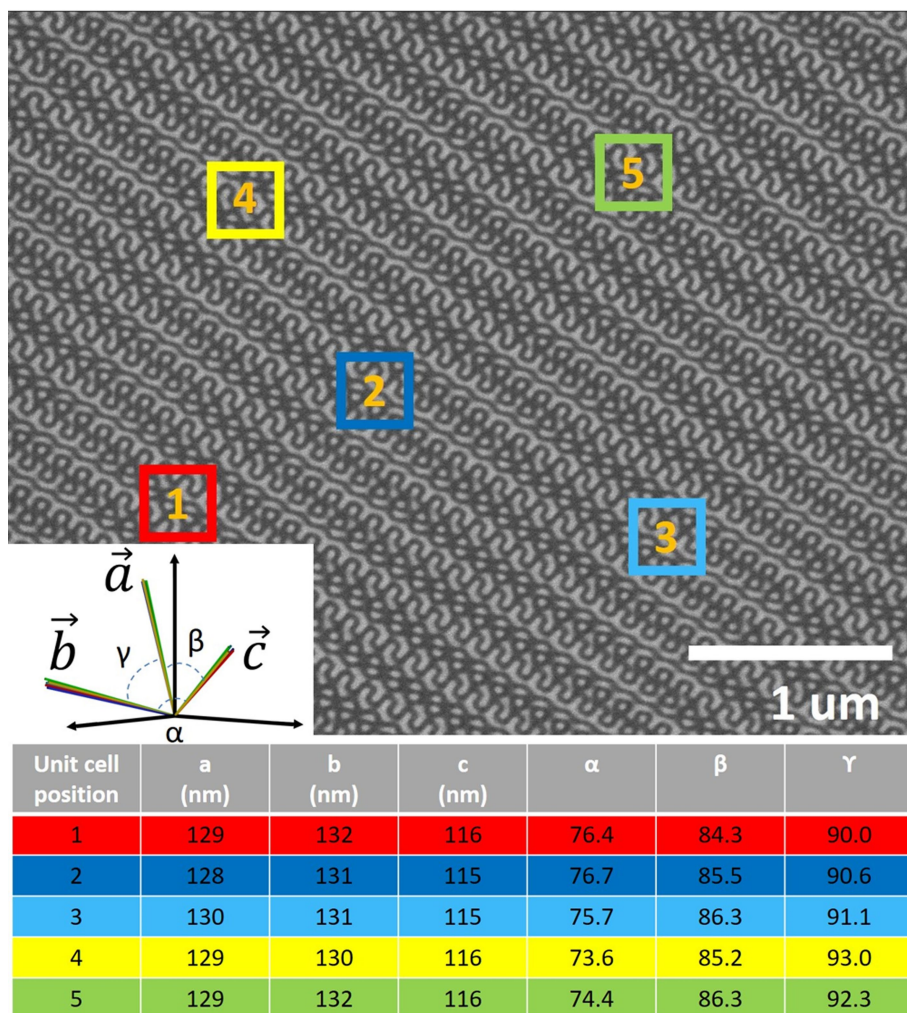
Author contributions The research was designed and supervised by E.L.T. and G.M.G. The BCP was synthesized by A.A., and R.-M.H. was responsible for processing samples. The SVSEM technique was developed by H.G., M.Z. and X.F., and carried out by X.F. and H.G. K.Y. provided modifications to the SVSEM software. Numerical algorithms for morphology analysis were developed by C.J.B. with I.P., and applied by C.J.B., X.F. and A.R. SCF computations were carried out and analysed by A.R. The manuscript was written by E.L.T, G.M.G., X.F., C.J.B. and A.R.

| Unit cell position	a (nm)	b (nm)	c (nm)	α	β	ϒ
1	129	132	116	76.4	84.3	90.0
2	128	131	115	76.7	85.5	90.6
3	130	131	115	75.7	86.3	91.1
4	129	130	116	73.6	85.2	93.0
5	129	132	116	74.4	86.3	92.3

Extended Data Fig. 1 | Variation in the unit-cell parameters of triclinic unit cells within one grain. Unit-cell parameters at five different places (1–5) within one grain are measured in real space. The result indicates that the structure is coherent but non-cubic, with unit-cell parameters exhibiting only small deviations throughout the many-cubic micrometre grain.
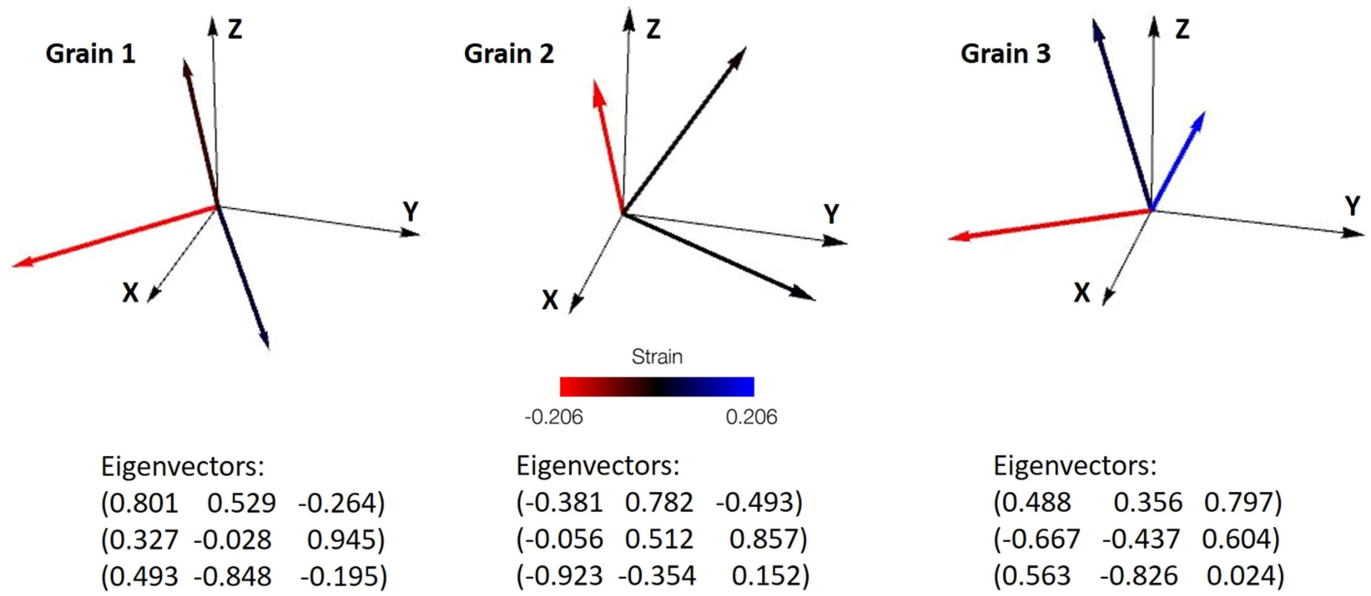
Extended Data Fig. 2 | Strain eigenvector mapping from a cDG lattice to a vtDG lattice within the slicing coordinate frame of reference. Directions and magnitudes of deviations from cubic symmetry in different grains of the sample are not correlated with the ion-milling (slicing) direction (*Z*).
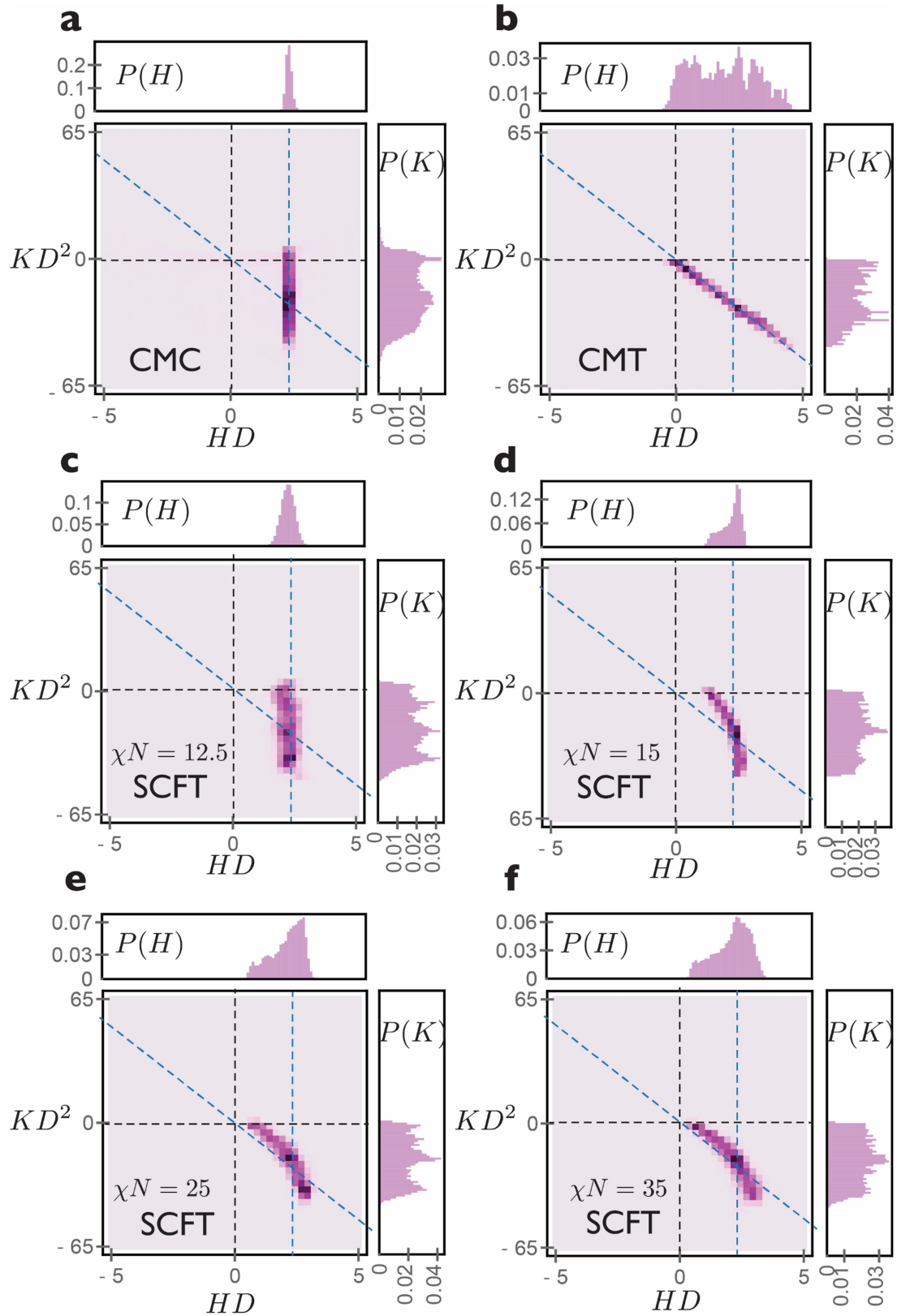
Extended Data Fig. 3 | Mean (H) and Gaussian (K) distribution of IMDS curvature in theoretical models. a, **b**, Distributions are shown for a constant mean curvature (CMC) surface (**a**) and for a constant matrix thickness (CMT) surface (**b**). **c**–**f**, Distributions obtained from SCF theoretical calculations of cDG as a function of segregation strength: $\chi N = 12.5$ (**c**), $\chi N = 15$ (**d**), $\chi N = 25$ (**e**) and $\chi N = 35$ (**f**). As in the main text, D is the cubic unit cell repeat length.
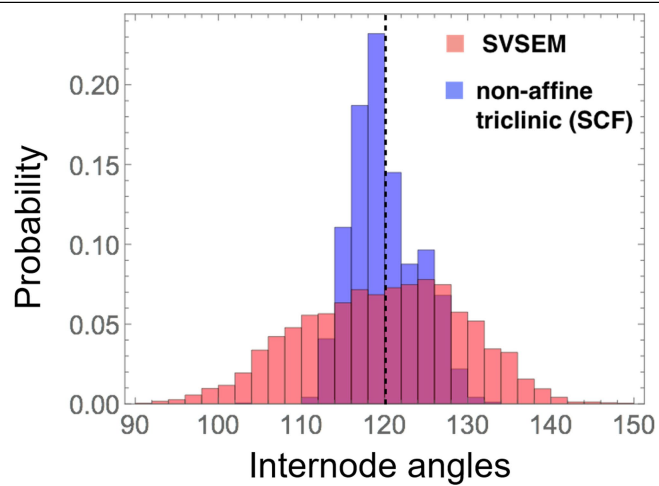
Extended Data Fig. 4 | Histogram showing the internode angles of experimental vtDG (from SVSEM) and non-affine triclinic SCF models.
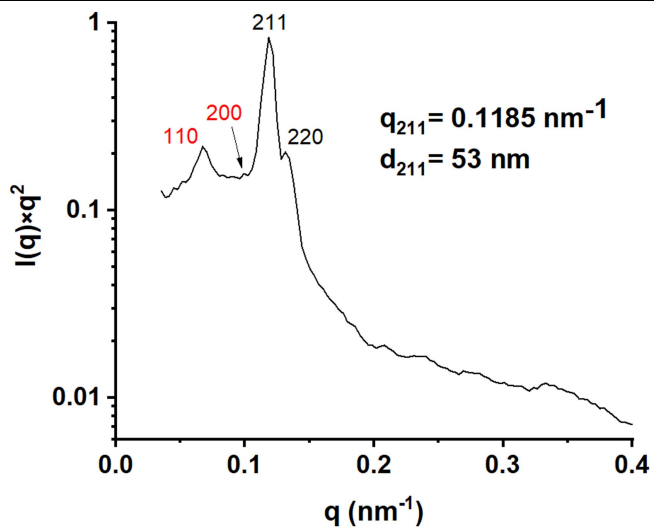
Extended Data Fig. 5 | SAXS pattern from a region of the bulk polygranular PS-PDMS sample. The structure can be nominally associated with a double-gyroid morphology, with an average cubic lattice parameter of $D = 130$ nm. Diffraction from the $\{110\}_{tDG}$ and $\{200\}_{tDG}$ families, which are forbidden for the cubic $Ia\bar{3}d$ space group, are observed, indicating the non-affine deformation of the cubic double-gyroid lattice.
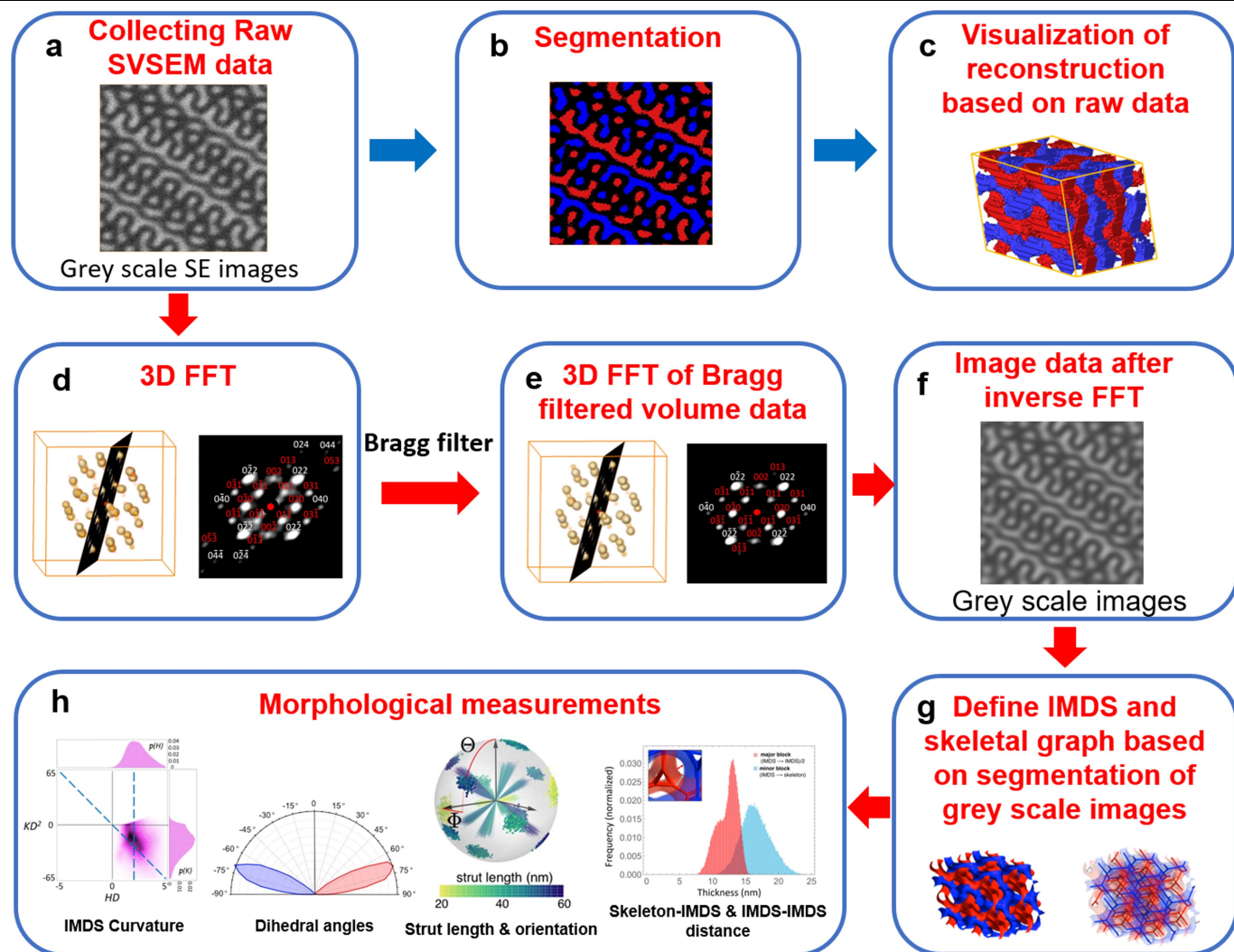
Extended Data Fig. 6 | The workflow for collection and analysis of SVSEM tomography data. See Methods for more details.

(a) Serial acquisition of High-resolution SEM images

1. Image (SEM)   2. Slicing (FIB)   3. Image (SEM)

Image Processing / Alignment

Ga⁺ ion beam

Electron beam   Electron beam

Stack of slices

(b)

e⁻

Ga⁺

Slicing surface

BCP specimen

45°   7°   Stage tilt

(i) Ion milling

e⁻

Ga⁺

Imaging surface

BCP specimen

45°   Increase stage tilt   45°

(ii) Electron imaging
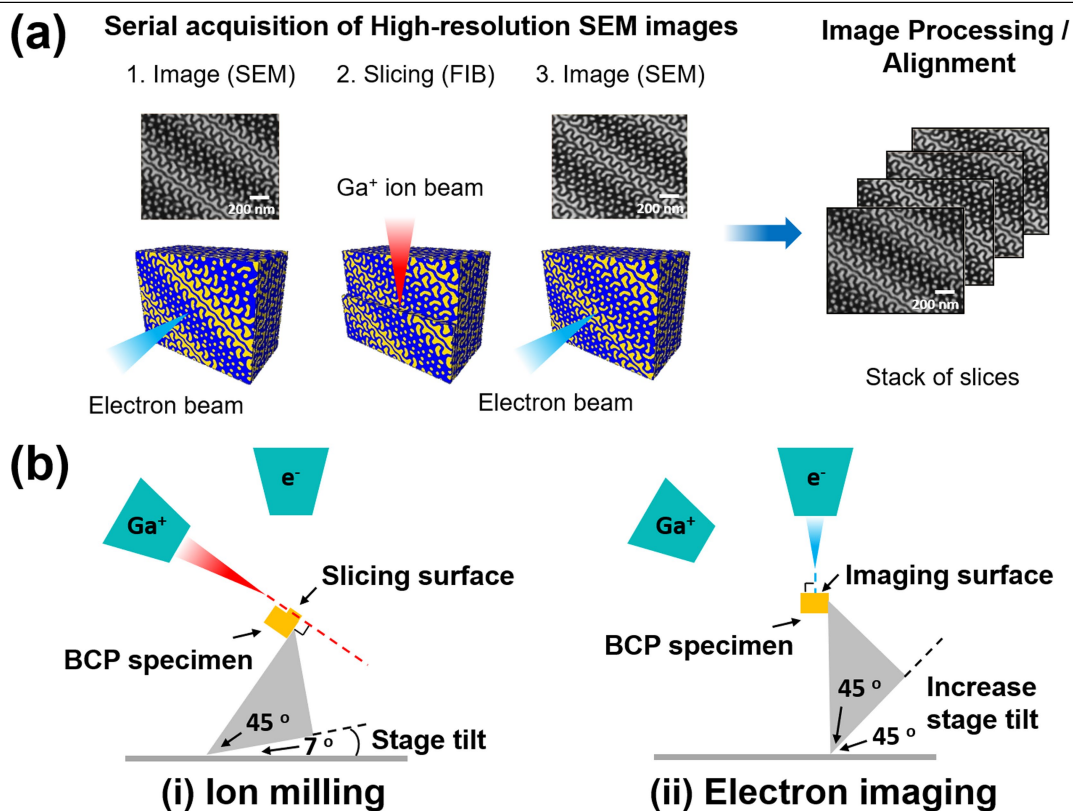
Extended Data Fig. 7 | Acquisition and processing of SVSEM images.
a, Illustration of the SVSEM reconstruction method. In step 1, low-energy incident electrons (1 KeV) are used to image the near-surface region of a bulk sample. In step 2, a Ga⁺ beam is used to slice a roughly 3-nm-thick section from the sample surface. In step 3, electrons are again used to image the ion-beam-milled sample surface. The process is repeated. With a large enough number of images (more than 200), the 3D morphology can be constructed via alignment of the stack of slices. **b**, Different sample stage positions are used for undistorted imaging during slice-and-view. **i**, For ion milling during slicing, the sample observing surface is parallel to the ion beam. **ii**, For electron imaging, the sample observing surface is perpendicular to the electron beam.
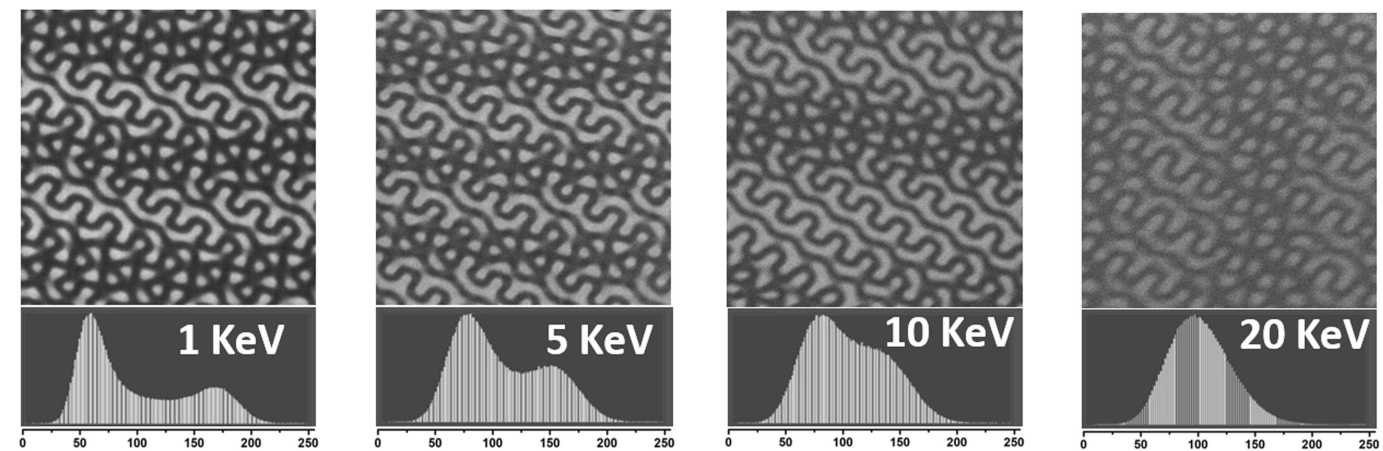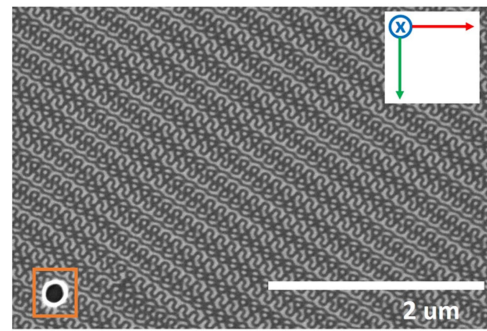
Extended Data Fig. 8 | Secondary-electron images acquired with different electron-accelerating voltages. Corresponding raw greyscale pixel-intensity distributions are presented blow the electron images. With a lower accelerating voltage, there is a clear binary separation of the pixels into a dark peak (left) and a bright peak (right). Each image is from a freshly sliced region.
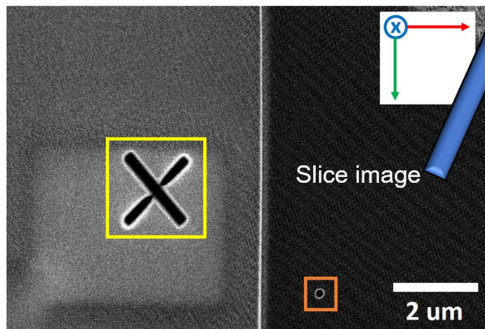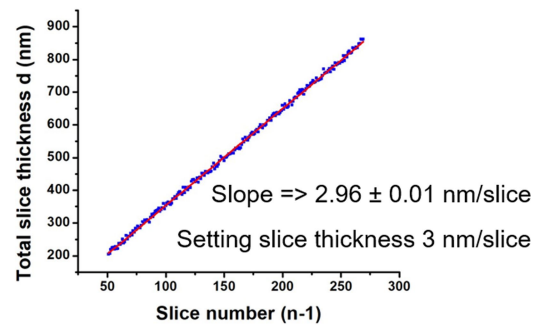
(a) FIB Image for registration

Ion beam along green vector
Electron beam along blue vector

Milling window

2 um

(b) SEM Image for registration

Slice image

2 um
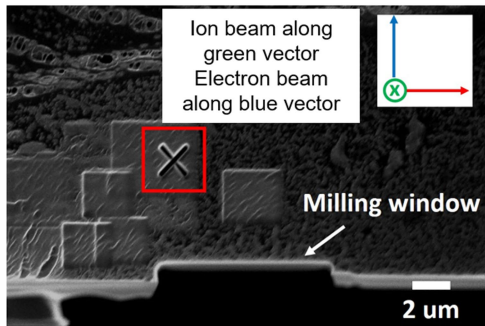
(c) SEM Image for data acquisition

2 um

**(d)** Monitoring the slice thickness


Slope => 2.96 ± 0.01 nm/slice

Setting slice thickness 3 nm/slice

Extended Data Fig. 9 | Alignment fiducials and monitoring of slice thickness during experiments. a, An X-shaped fiducial (within the red square) in ion-beam view is used for the registration of FIB slicing. **b**, An X-shaped fiducial (within the yellow square) in electron-beam view is used for registration of electron imaging. The round cross-section of the perpendicularly drilled hole (within the orange square) is used for the fine registration of secondary-electron images. **c**, A secondary-electron image used for data acquisition, showing an ion-milled hole (within the orange square) used for fine registration. **d**, Monitoring of slice thickness: we measured the distance between the milling surface of the nth slice and the milling surface of the first slice (total slice thickness d) from FIB images, and then plotted d versus ($n − 1$). This reveals a linear relationship with a slope of $2.96 ± 0.01$, which is the averaged slice thickness (in nm).
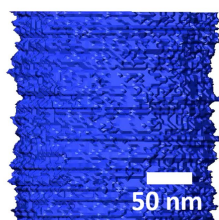
(a)

(b)   **(c)**
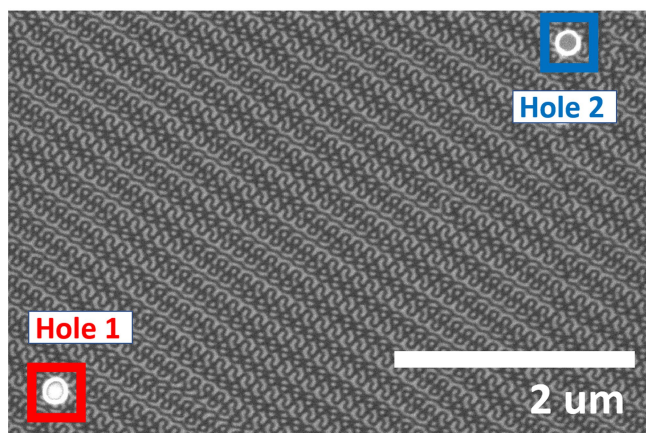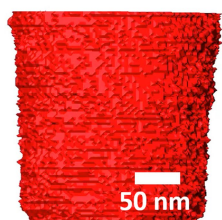
Hole 1   **Hole 2**

Extended Data Fig. 10 | Monitoring of potential SEM image rotation during FIB-SEM image collection. a, SEM raw data image of the region of interest, with two holes drilled normal to the slice surface by the FIB. **b**, **c**, Side-view snapshots of 3D reconstructed holes 1 and 2 (the corresponding rotational videos are in Supporting Video 3). The image stack (80 slices) was aligned using hole 1. The reconstruction of hole 2 is still symmetric, indicating no image rotation.
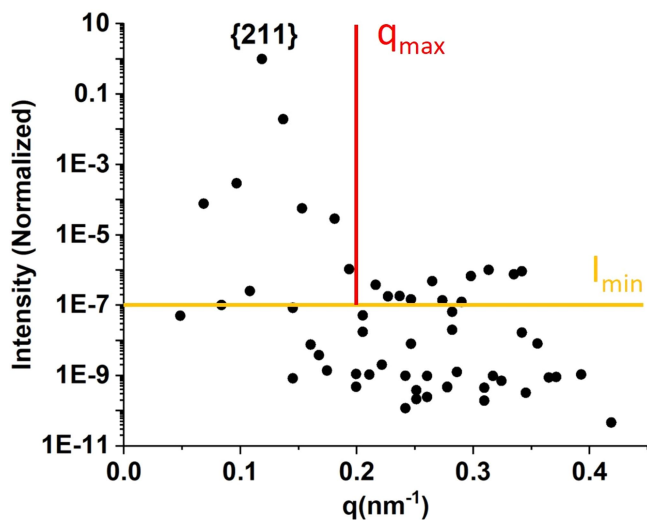
Extended Data Fig. 11 | Important Fourier components of the experimental double-gyroid structure. The overall intensity of each diffraction family was normalized by the strongest $\{211\}_{tDG}$ family from the 3D FFT of the region containing approximately 160 unit cells (the same region as in Fig. 4f, which shows the intensity of each individual peak). The overall normalized intensity data are plotted against their associated cubic q value for those planes. For our reconstructions, we use a Bragg filter that selects peaks above an intensity threshold of 10^{-7} (I_{min}) for associated q values smaller than $0.2\,nm^{-1}$.